Look-ahead Dispatch of Power Systems Based on Linear Alternating Current Optimal Power Flow Framework with Nonlinear Frequency Constraints Using Physics-informed Neural Networks

Guoqiang Sun, Qihui Wang, Sheng Chen, Zhinong Wei, and Haixiang Zang

***Abstract*—The increasing penetration of renewable energy resources degrades the frequency stability of power systems. The present work addresses this issue by proposing a look-ahead dispatch model of power systems based on a linear alternating current optimal power flow framework with nonlinear frequency constraints. Meanwhile, the poor efficiency for solving this formulation is addressed by introducing a physics-informed neural network (PINN) to predict key frequency-control parameter values accurately. The PINN ensures that the learned results are applicable to the original physical frequency dynamics model, and applying the predicted parameter values enables the resulting dispatch model to be solved quickly and efficiently using readily available commercial solvers. The feasibility and advantages of the proposed model are demonstrated by the results of numerical computations applied to a modified IEEE 118-bus test system.**

***Index Terms*—Frequency stability, physics-informed neural network, optimal power flow (OPF), loss function, frequency constraint, look-ahead dispatch.**

NOMENCLATURE

A. Indices and Sets

Ω_i^G	Set of thermal generators connected at bus i
Ω_i^W	Set of wind farms connected at bus i
Ω_i^{PV}, Ω_i^{ESS}	Sets of photovoltaic (PV) stations and energy storage stations (ESSs) connected at bus i
$\sigma(i)$	Set of transmission lines associated with node i
es	ESS index (1 to total ESSs N_{ESS})
g	Thermal generator indexes (1 to total generators N_G)
m	Number of training data points (1 to total points M)
n,i,j	Bus node index (1 to total buses N_n)
pv	PV station index (1 to total PV stations N_{PV})
t	Time index (1 to full period T)
w	Wind farm index (1 to total wind farms N_W)

B. Parameters

α_1, α_2, α_3, α_4	Corresponding weights applied to each of above-defined penalty terms
$\Delta f_{\max}$	The maximum allowable frequency deviation
Δf_{ss}	The maximum allowable steady-state frequency deviation
ΔP	Imaginary power disturbance
Δt	Scheduling time interval
$\theta_{ij}^{\max}, \theta_{ij}^{\min}$	The maximum and minimum values of phase angle difference between node i and node j
η_{es}^C, η_{es}^D	Charge and discharge efficiencies of ESS es
C_g	Variable operation cost of thermal generator g
$C_g^{reserve}$	Flexible reserve cost of thermal generator g
$C_w^{reserve}$	Flexible reserve cost of wind farm w
$C_{es}^{reserve}$	Flexible reserve cost of ESS es
$C_{pv}^{reserve}$	Flexible reserve cost of PV station pv
D	Damping factor
$E_{es}^{\max}, E_{es}^{\min}$	Upper and lower state of charge (SoC) bounds of ESS es
F_g	Fraction of power generated by thermal generator g
f_0	Nominal frequency
G_{ij}, B_{ij}	Real and imaginary parts of Y_{ij} in admittance matrix
g_{ij}, b_{ij}	Conductance and susceptance of branch ij
$H_{g,t}$	Virtual inertia of thermal generator g at time t

Manuscript received: April 29, 2024; revised: May 27, 2024; accepted: June 8, 2024. Date of CrossCheck: June 8, 2024. Date of online publication: August 20, 2024.

This work was supported by the National Natural Science Foundation of China (No. 52077060).

G. Sun, Q. Wang, S. Chen (corresponding author), Z. Wei, and H. Zang are with the School of Electrical and Power Engineering, Hohai University, Nanjing 210098, China (e-mail: hhusunguoqiang@163. com; wangqihui_hhu@163. com; chenshenghhu@163.com; wzn_nj@263.net; zanghaixiang@hhu.edu.cn).

DOI: 10.35833/MPCE.2024.000452

$H_w^{\max}, H_w^{\min}$ Upper and lower virtual inertia bounds of wind farm w

$H_{pv}^{\max}, H_{pv}^{\min}$ Upper and lower virtual inertia bounds of PV station pv

$H_{es}^{\max}, H_{es}^{\min}$ Upper and lower virtual inertia bounds of ESS es

K_{mg} Mechanical power gain factor

$P_{g,t}^{\max}, P_{g,t}^{\min}$ The maximum and minimum active power outputs of thermal generator g at time t

$P_{d,i}, Q_{d,i}$ Active and reactive load demands d at node i

$P_{w,t}^{History}$ Historical power output of wind farm w at time t

$P_{pv,t}^{History}$ Historical power output of PV station pv at time t

$P_{es,t}^{\max}$ Upper charge/discharge power bound of ESS es at time t

$Q_g^{\max}, Q_g^{\min}$ The maximum and minimum reactive power outputs of thermal generator g

R Governor regulation constant

R_g Governor regulation constant of thermal generator g

RU_g, RD_g Hourly ramp up and down capacities of thermal generator g

$R_w^{\max}, R_w^{\min}$ Upper and lower droop coefficient bounds of wind farm w

$R_{pv}^{\max}, R_{pv}^{\min}$ Upper and lower droop coefficient bounds of PV station pv

$R_{es}^{\max}, R_{es}^{\min}$ Upper and lower droop coefficient bounds of ESS es

$S_{ij}^{\max}$ Capacity of transmission line between node i and node j

T_R Reheat time constant

t_{nadir} Time to reach the lowest frequency

$v_i^{\max}, v_i^{\min}$ The maximum and minimum voltage amplitudes at node i

v_0, θ_0 Values of v and θ in basic case

y_m Actual value of the m^{th} data point

$\hat{y}_m$ Estimated value of the m^{th} data point

C. Variables

θ_i Voltage angle at node i

θ_{ij} Phase angle difference between node i and node j

C_{total} System total operation cost

$E_{es,t}$ SoC of ESS es at time t

F_t System-equivalent turbine parameter at time t

H_t System-equivalent inertia constant at time t

$H_{es,t}$ Virtual inertia of ESS es at time t

$H_{w,t}$ Virtual inertia of wind farm w at time t

$H_{pv,t}$ Virtual inertia of PV station pv at time t

$L_{es,t}^C, L_{es,t}^D$ Charge and discharge power losses of ESS es at time t

$L_{es,t}$ Power loss of ESS es at time t

$L_{ij}^{u,nn}$, $L_{ij}^{d,\mathrm{mm}}$ Intermediate variables

P_{ij}^{appro} Linear approximation of active power flow

$P_{ij}^{loss}, Q_{ij}^{loss}$ Active and reactive power losses of branch ij

P_g, Q_g Active and reactive power outputs of thermal generator g

P_i, Q_i Active and reactive power injections at bus i

P_{ij}, Q_{ij} Active and reactive power flows from bus i to bus j

$P_{g,t}^{reserve}$ Backup power of thermal generator g at time t

$P_{w,t}^{reserve}$ Backup power of wind farm w at time t

$P_{pv,t}^{reserve}$ Backup power of PV station pv at time t

$P_{es,t}^{reserve}$ Backup power of ESS es at time t

$P_{w,t}, P_{pv,t}$ Power outputs of wind farm w and PV station pv at time t

$P_{es,t}$ Power output of ESS es at time t

Q_{ij}^{appro} Linear approximation of reactive power flow

R_t System-equivalent governor regulation constant at time t

$R_{es,t}$ Droop coefficient of ESS es at time t

$R_{w,t}$ Droop coefficient of wind farm w at time t

$R_{pv,t}$ Droop coefficient of PV station pv at time t

v_i, v_j Voltage amplitudes at node i and node j

I. Introduction

THE increasing demand for alternative energy technologies in recent years has been progressively replacing the conventional rotational generation facilities in power systems with an increasing proportion of renewable energy sources (RESs) such as wind and photovoltaic (PV) power [1]. However, this development gradually decreases the rotational inertia of power systems, and thereby increasingly promotes the problem of frequency stability during power system dispatch [2], [3]. Hence, frequency response constraints have been incorporated into a number of power system dispatch models [4]-[6]. In addition, RESs will also need to provide frequency regulation support in the future [7], [8]. However, conventional economic dispatch is unable to account for the dynamic changes in frequency that must be considered for meeting the frequency stability requirements of power systems with a high proportion of RESs. At the same time, since the prediction errors of RESs significantly increase as the time scale grows, short-term scheduling becomes crucial. This has led to the increased development of look-ahead dispatch models in recent years, which typically schedule resources at 15-min time intervals.

The intra-day look-ahead dispatch [9] has been introduced as a bridge between day-ahead unit commitment (UC) [10], [11] and real-time scheduling. Reference [12] introduces an efficient robust look-ahead dispatch scheme that includes critical region preparation during gap time to enhance the computational efficiency of the robust look-ahead dispatch. Reference [13] suggests defining the distributionally robust conditional value-at-risk with uncertain constraints. Additionally, a scalable robust optimization program is utilized to generate an approximation of distributionally robust chance-constrained look-ahead economic dispatch. The main drawback associated with the short scheduling window of look-ahead dispatch models is that the model must be solved in seconds. As a result, many existing look-ahead dispatch models developed for power systems with frequency constraints have applied quickly solvable linear direct current optimal power flow (DC-OPF) formulations [14]-[16]. However, the dispatch model is made linear by ignoring the reactive power, assuming a flat voltage magnitude for all buses [17]. As a result, the system voltage can exceed the safe operation range under the applied dispatch, which is a significant threat to the safe and stable operation of the power system. Therefore, linear DC-OPF obviously cannot meet the demand for voltage stability in power systems. Nonetheless, directly applying an alternating current optimal power flow (AC-OPF) formulation is too cumbersome. Recent efforts to address this issue include the development of a linearized AC-OPF model [18]. However, applying a linearized AC-OPF formulation in the dispatch model is not sufficient to guarantee adequate solution speed.

Among existing efforts to improve the efficiency for solving look-ahead dispatch models, the use of deep neural networks (DNNs) is demonstrated to be promising for providing data-driven solutions with limited computational resources to physics-related problems like dispatch models in which the physical mechanism is not fully understood [19], [20]. Moreover, neural networks are being increasingly applied in power systems with the increasing development of deep learning (DL) [21]-[23]. Nevertheless, the extension of DL approaches within the domain of power systems has encountered a number of challenges such as high requirements for the quality and quantity of training data, the production of physically infeasible or inconsistent solutions, and the low generalization ability and interpretability of DNN models.

The frequency control parameters enabling RES unit themselves to provide frequency regulation support to power systems are designed according to the modeled frequency dynamics of the power system. Currently, this modeling is conducted based on a derivation of the low-order frequency response model of the power system [24]. However, the process is greatly complicated by the fact that power systems are composed of many conventional generator units and RES units. Reference [25] addresses this issue by developing an analytical approach for aggregating the frequency response of multiple units into a single-unit model. Reference [26] is one of the first research to include frequency regulation constraints in the UC model of a power system. However, while this study ensures the adequacy of primary and tertiary frequency reserves, it considers only the quasi-steady-state frequency of the power system. Reference [27] proposes a frequency-constrained UC model based on a frequency security margin defined as the maximum power imbalance that can be sustained by the power system while maintaining the frequency within a tolerable range. Reference [28] proposes an enhanced frequency-constrained UC model considering variable-droop frequency control from converter-based generators. Reference [29] presents a frequency-constrained stochastic dispatch approach for power systems with high proportions of RES generation. However, these past studies based on the use of frequency constraints in the UC problem tend to provide poor frequency and voltage stability under a high proportion of RESs. In order to further improve the frequency stability of the power system, solution efficiency is enhanced in [14] by proposing a frequency-constrained OPF-based stochastic look-ahead dispatch model that applies virtual inertia parameters and droop control coefficients for RES and energy storage system (ESS) units as variables for online rolling dispatch optimization. In addition, [30] proposes an OPF-based model, which formulates the dynamic frequency response of the power system as a set of differential equations, and frequency stability is obtained by applying dynamic frequency response constraints when re-dispatching generation units. However, these models employ DC-OPF formulations to ensure rapid convergence and fast computation speed. Moreover, frequency-dependent constraints are highly nonlinear, and conventional model-based optimization approaches are difficult to solve efficiently.

Despite the challenges associated with extending DL approaches within the domain of power systems, a number of studies have greatly increased the speed with which solutions can be obtained for dispatch models applied to large-scale power systems. For example, [23] proposes an embedded approach for training a DNN to solve multiple AC-OPF problems with flexible topology and line admittances, and the solution speed is increased by three orders of magnitude compared with that using a solver to solve the physical model for a large-scale power system composed of 2000 buses. Reference [31] applies a gated recurrent unit (GRU) neural network to map relationships between system daily loads and dispatch decision results, thereby achieving solutions to a security-constrained UC problem. However, the DL approaches developed in these studies cannot guarantee that the trained networks can satisfy all the constraints in the original model. In addition to the high training data requirements, physically infeasible/inconsistent outcomes, and the low generalization ability and interpretability of DNN models, a serious issue is represented to limit the application of DL approaches for solving dispatch models.

One state-of-the-art approach addressing these shortcomings in DL approaches involves the incorporation of known physical laws that govern a given dataset in the learning process using physics-informed neural networks (PINNs) [32]. For example, [33] applies a PINN to estimate solutions to an AC-OPF model accurately. Reference [34] applies a PINN to solve an OPF model. Reference [35] regularizes a physics-guided neural network to calculate the load margin of power systems. However, the above approaches have only been applied to relatively simple models such as the OPF model, and there has been little research that applies a PINN to the models with strong comprehensiveness. In this paper, we address the above discussed issues by proposing a look-ahead dispatch model of power systems based on a linear AC-OPF framework with nonlinear frequency constraints. The efficiency of the model solution process is enhanced under the nonlinear frequency constraints by applying a PINN-assisted approach. The main contributions are summarized as follows.

1) The proposed model ensures practical real-time frequency-controlled operation by co-optimizing the virtual inertia parameters and droop control coefficients applied for RES and ESS units.

2) The profoundly negative impact of the nonlinear frequency constraints on the solution process is addressed by applying a PINN to predict the virtual inertia parameters and droop coefficients of RES and ESS units based on the active power demands, reactive power demands, RES outputs, and commitment states of thermal generators, which are employed as penalty terms in the loss function applied for training the PINN. In contrast to the use of a conventional DNN, the PINN ensures that the learned results are applicable to the original physical frequency dynamics model of the power system. In addition, the application of these predicted terms transforms the proposed model into a Quadratic constrained programming (QCP) model with quadratic terms only in the objective function and all other constraints being linear constraints, which can be solved quickly and efficiently using readily available commercial solvers.

3) The results of numerical computations applied to a modified IEEE 118-bus test system (denoted as test system) demonstrate that the proposed model can reduce operation costs while ensuring frequency safety under small power disturbances. Meanwhile, the frequency safety can be ensured under large power disturbances with very modest cost increases by adjusting the virtual inertia and droop control coefficients of RESs and ESSs. Moreover, the PINN-assisted approach is demonstrated to improve the solution efficiency greatly compared with model-assisted solution approaches, and reduces the number of violations in the frequency security constraints compared with a DNN-assisted approach.

The remainder of this paper is organized as follows. Section II introduces the model framework and frequency constraints. Section III presents the solution methodology. The results of the case studies are presented in Section IV. Finally, conclusions are drawn in Section V.

II. Model Framework and Frequency Constraints

In this section, we first introduce the linear AC-OPF framework. Then, the nonlinear frequency constraints are provided in detail. Finally, we present a look-ahead dispatch model for the power system that integrates linear AC-OPF while considering frequency security constraints.

A. Linear AC-OPF Framework

The standard linear AC-OPF framework can be formulated as:

$$\min \sum_{g=1}^{N_G} C_g P_g \tag{1}$$

$$P_i = \sum_{g \in \Omega_i^G} P_g - P_{d,i} = \sum_{j \in \sigma(i)} P_{ij} + \left(\sum_{j=1}^{N_n} G_{ij} \right) v_i^2 \quad i \in N_n \tag{2}$$

$$Q_i = \sum_{g \in \Omega_i^G} Q_g - Q_{d,i} = \sum_{j \in \sigma(i)} Q_{ij} + \left(\sum_{j=1}^{N_n} -B_{ij} \right) v_i^2 \quad i \in N_n \tag{3}$$

$$P_{ij} = g_{ij}\left(v_i^2 - v_i v_j \cos\theta_{ij} \right) - b_{ij} v_i v_j \sin\theta_{ij} \tag{4}$$

$$Q_{ij} = -b_{ij}\left(v_i^2 - v_i v_j \cos\theta_{ij} \right) - g_{ij} v_i v_j \sin\theta_{ij} \tag{5}$$

$$P_g^{\min} \le P_g \le P_g^{\max} \quad g \in N_G \tag{6}$$

$$Q_g^{\min} \le Q_g \le Q_g^{\max} \quad g \in N_G \tag{7}$$

$$v_i^{\min} \le v_i \le v_i^{\max} \quad i \in N_n \tag{8}$$

$$P_{ij}^2 + Q_{ij}^2 \le \left(S_{ij}^{\max} \right)^2 \tag{9}$$

$$\theta_{ij}^{\min} \le \theta_{ij} \le \theta_{ij}^{\max} \tag{10}$$

Objective function (1) aims to minimize the total generation cost. Constraints (2) and (3) are the nodal active and reactive power balance equations, respectively. Constraints (4) and (5) govern the branch flows. The minimum and maximum limits on the active and reactive power of each generator are enforced by constraints (6) and (7), respectively. Constraint (8) limits the voltage magnitude at each bus. Constraints (9) and (10) restrict the branch flows and voltage phase angles, respectively. It is evident that constraints (2)-(5) and (9) in the above AC-OPF framework are nonlinear. Therefore, this framework can be linearized by converting these constraints into linear constraints. As provided in [18] and [36], the following two assumptions are made: ① the value of θ_{ij} is relatively small; and ② the magnitude of v is close to 1.0 p.u..

Thus, the following equations are obtained as:

$$P_{ij}^{appro} = g_{ij} \frac{v_i^2 - v_j^2}{2} - b_{ij}\theta_{ij} + P_{ij}^{loss} \tag{11}$$

$$Q_{ij}^{appro} = -b_{ij} \frac{v_i^2 - v_j^2}{2} - g_{ij}\theta_{ij} + Q_{ij}^{loss} \tag{12}$$

Here, the following loss terms have been applied.

$$P_{ij}^{loss} = g_{ij}\theta_{ij,0}\theta_{ij} - \frac{1}{2} g_{ij}\theta_{ij,0}^2 + g_{ij}\frac{v_{i,0} - v_{j,0}}{v_{i,0} + v_{j,0}}\left(v_i^2 - v_j^2 \right) - \frac{g_{ij}}{2}\left(v_{i,0} - v_{j,0} \right)^2 \tag{13}$$

$$Q_{ij}^{loss} = -b_{ij}\theta_{ij,0}\theta_{ij} + \frac{1}{2} b_{ij}\theta_{ij,0}^2 - b_{ij}\frac{v_{i,0} - v_{j,0}}{v_{i,0} + v_{j,0}}\left(v_i^2 - v_j^2 \right) + \frac{b_{ij}}{2}\left(v_{i,0} - v_{j,0} \right)^2 \tag{14}$$

As is observed in constraints (2) and (3), constraints (11) and (12) as well as their corresponding loss terms (13) and (14) can be considered as linear constraints with respect to v^2. Constraint (9) is transformed using the piecewise linearization approach [37], [38]. The derivation of constraints (9)-(15) is provided in Supplementary Material A.

$$\begin{cases} \Lambda\left(P_{ij}^{appro}, Q_{ij}^{appro} \right) & L_{ij}^{u,nn} \ge 0 \quad nn = 1, 2, \ldots, NN \\ \Lambda\left(P_{ij}^{appro}, Q_{ij}^{appro} \right) & L_{ij}^{d,mm} \ge 0 \quad mm = 1, 2, \ldots, MM \end{cases} \tag{15}$$

Accordingly, objective function (1) and constraints (2), (3), (6)-(8), and (10)-(15) constitute linear AC-OPF model.

B. Frequency Constraints

The following analytical expression of the frequency dynamics after a step disturbance ΔP, e.g., the maximum thermal generator output or the tie-line capacity, can be obtained according to a previously proposed aggregated system frequency model [25].

$$\Delta f(t)=\frac{R\Delta P}{DR+1}\left(1+\alpha \mathrm{e}^{-\zeta\omega_n t}\sin\left(\omega_r t+\varphi\right)\right) \tag{16}$$

The following previously defined terms have been applied.

$$\alpha=\sqrt{\frac{1-2T_R\zeta\omega_n+T_R^2\omega_n^2}{1-\zeta^2}} \tag{17}$$

$$\zeta=\frac{DRT_R+2HR+FT_R}{2(DR+1)}\omega_n \tag{18}$$

$$\omega_n^2=\frac{DR+1}{2HRT_R} \tag{19}$$

$$\omega_r=\omega_n\sqrt{1-\zeta^2} \tag{20}$$

$$\varphi=\arctan\left(\frac{\omega_r T_R}{1-\zeta\omega_n T_R}\right)-\arctan\left(\frac{\sqrt{1-\zeta^2}}{-\zeta}\right) \tag{21}$$

The detailed physical meanings of H, ω_n, α, ζ, and φ can be found in [25]. Taking the derivative of (16) with respect to time and setting $f'(t)=0$ yield the following expressions for frequency deviation corresponding to frequency nadir due to ΔP.

$$t_{nadir}=\frac{1}{\omega_r}\arctan\left(\frac{\omega_r T_R}{\zeta\omega_r T_R-1}\right) \tag{22}$$

$$\Delta f_{nadir}=\frac{R\Delta P}{DR+1}\left(1+\sqrt{1-\zeta^2}\,\alpha \mathrm{e}^{-\zeta\omega_n t_{nadir}}\right) \tag{23}$$

In addition, we note that $\Delta f(t)=R\Delta P/(DR+1)$ when $t\rightarrow\infty$. Therefore, the frequency nadir and steady-state frequency constraints of the system can be written as:

$$\frac{R\Delta P}{DR+1}\left(1+\sqrt{1-\zeta^2}\,\alpha \mathrm{e}^{-\zeta\omega_n t_{nadir}}\right)\le\Delta f_{\max} \tag{24}$$

$$\frac{R\Delta P}{DR+1}\le\Delta f_{ss} \tag{25}$$

The expressions for parameters H, R, and F are defined as:

$$H_t=\frac{1}{\sum_i P_{d,i,t}}\left(\sum_{es}H_{es,t}P_{es,t}^{\max}+\sum_g H_{g,t}P_{g,t}^{\max}+\sum_w H_{w,t}P_{w,t}^{History}+\sum_{pv}H_{pv,t}P_{pv,t}^{History}\right) \tag{26}$$

$$\frac{1}{R_t}=\frac{1}{\sum_i P_{d,i,t}}\left(\sum_g\frac{K_{mg}}{R_g}P_{g,t}^{\max}+\sum_{es}\frac{1}{R_{es,t}}P_{es,t}^{\max}+\sum_w\frac{1}{R_{w,t}}P_{w,t}^{History}+\sum_{pv}\frac{1}{R_{pv,t}}P_{pv,t}^{History}\right) \tag{27}$$

$$F_t=\frac{1}{\sum_i P_{d,i,t}}\left(\sum_g\frac{K_{mg}F_g}{R_g}P_{g,t}^{\max}\right) \tag{28}$$

Finally, the reserve constraints for RESs and ESSs are:

$$P_{w,t}^{reserve}\ge\frac{P_{w,t}^{History}}{R_{w,t}}\frac{\Delta f_{\max}}{f_0}+2H_{w,t}P_{w,t}^{History}\frac{\Delta f_{ss}}{f_0} \tag{29}$$

$$P_{pv,t}^{reserve}\ge\frac{P_{pv,t}^{History}}{R_{pv,t}}\frac{\Delta f_{\max}}{f_0}+2H_{pv,t}P_{pv,t}^{History}\frac{\Delta f_{ss}}{f_0} \tag{30}$$

$$P_{es,t}^{reserve}\ge\frac{P_{es,t}^{\max}}{R_{es,t}}\frac{\Delta f_{\max}}{f_0}+2H_{es,t}P_{es,t}^{\max}\frac{\Delta f_{ss}}{f_0} \tag{31}$$

C. Look-ahead Dispatch Model

The look-ahead dispatch model based on the linear AC-OPF framework presented above in conjunction with the proposed frequency constraints can be given as:

$$\begin{aligned}\min C_{\text{total}}=&\sum_{t=1}^{T}\sum_{g=1}^{N_G}\left(P_{g,t}C_g+P_{g,t}^{reserve}C_g^{reserve}\right)+\\&\sum_{t=1}^{T}\sum_{w=1}^{N_W}\frac{\left(P_{w,t}^{reserve}\right)^2C_w^{reserve}}{P_{w,t}^{History}}+\sum_{t=1}^{T}\sum_{pv=1}^{N_{PV}}\frac{\left(P_{pv,t}^{reserve}\right)^2C_{pv}^{reserve}}{P_{pv,t}^{History}}+\\&\sum_{t=1}^{T}\sum_{es=1}^{N_{ESS}}\left(\frac{\left(P_{es,t}^{reserve}\right)^2C_{es}^{reserve}}{P_{es,t}^{\max}}+L_{es,t}\right)\end{aligned} \tag{32}$$

$$\begin{aligned}&\sum_{g\in\Omega_i^G}P_{g,t}+\sum_{w\in\Omega_i^W}P_{w,t}+\sum_{pv\in\Omega_i^{PV}}P_{pv,t}+\sum_{es\in\Omega_i^{ESS}}P_{es,t}=\\&\qquad P_{d,i,t}+\sum_{j\in\sigma(i)}P_{ij,t}^{appro}+\left(\sum_{j=1}^{N_n}G_{ij}\right)v_{i,t}^2\end{aligned} \tag{33}$$

$$\sum_{g\in\Omega_i^G}Q_{g,t}=Q_{d,i,t}+\sum_{j\in\sigma(i)}Q_{ij,t}^{appro}+\left(\sum_{j=1}^{N_n}-B_{ij}\right)v_{i,t}^2 \tag{34}$$

$$-RD_g\le P_{g,t}-P_{g,t-1}\le RU_g \tag{35}$$

$$P_{g,t}^{\min}\le P_{g,t}\le P_{g,t}^{\max} \tag{36}$$

$$Q_{g,t}^{\min}\le Q_{g,t}\le Q_{g,t}^{\max} \tag{37}$$

$$P_{g,t}+P_{g,t}^{reserve}\le P_{g,t}^{\max} \tag{38}$$

$$P_{w,t}+P_{w,t}^{reserve}\le P_{w,t}^{History} \tag{39}$$

$$P_{pv,t}+P_{pv,t}^{reserve}\le P_{pv,t}^{History} \tag{40}$$

$$P_{es,t}+P_{es,t}^{reserve}\le P_{es,t}^{\max} \tag{41}$$

$$0\le P_{pv,t}\le P_{pv,t}^{History} \tag{42}$$

$$0\le P_{w,t}\le P_{w,t}^{History} \tag{43}$$

$$-P_{es,t}^{\max}\le P_{es,t}\le P_{es,t}^{\max} \tag{44}$$

$$P_{g,t}^{reserve}\ge\frac{P_{g,t}^{\max}}{R_g}\frac{\Delta f_{ss}}{f_0} \tag{45}$$

$$L_{es,t}\ge L_{es,t}^D \tag{46}$$

$$L_{es,t}\ge L_{es,t}^C \tag{47}$$

$$L_{es,t}^C=\left(\eta_{es}^C-1\right)P_{es,t} \tag{48}$$

$$L_{es,t}^D=\left(\frac{1}{\eta_{es}^D}-1\right)P_{es,t} \tag{49}$$

$$E_{es,t}=E_{es,t-1}-\left(P_{es,t}+L_{es,t}\right)\Delta t \tag{50}$$

$$E_{es}^{\min}\le E_{es,t}\le E_{es}^{\max} \tag{51}$$

$$\begin{cases} H_w^{\min} \le H_{w,t} \le H_w^{\max} \\ R_w^{\min} \le R_{w,t} \le R_w^{\max} \end{cases} \tag{52}$$

$$\begin{cases} H_{pv}^{\min} \le H_{pv,t} \le H_{pv}^{\max} \\ R_{pv}^{\min} \le R_{pv,t} \le R_{pv}^{\max} \end{cases} \tag{53}$$

$$\begin{cases} H_{es}^{\min} \le H_{es,t} \le H_{es}^{\max} \\ R_{es}^{\min} \le R_{es,t} \le R_{es}^{\max} \end{cases} \tag{54}$$

$$\text{Constraints (11)-(15), (17)-(22), (24)-(31)} \tag{55}$$

Objective function (32) seeks to minimize the operation cost of the power system, including the variable operation costs of the thermal generators and reserve cost, and the power losses of ESSs. Constraints (33) and (34) represent nodal power balance equations. Constraint (35) restricts the ramping rates of thermal generators. Constraints (36) and (37) limit the output power of thermal generators. Constraints (38) and (45) limit the reserve capacity of thermal generators. Constraints (29)-(31) and (39)-(41) restrict the backup capacities of RESs and ESSs. Constraints (42)-(44) limit the power outputs of PV, wind, and ESS units, respectively. Constraints (46) and (47) restrict the power losses of ESSs. Constraints (48) and (49) define acceptable power losses for ESS units during charge and discharge, respectively. Constraints (50) and (51) restrict the state of charge (SoC) for ESS units. Constraints (52)-(54) limit the allowable adjustment ranges for the virtual inertia parameters and droop coefficients of RES and ESS units.

III. Solution Methodology

This section elaborates on the construction of the loss function in PINN and provides the structural diagram of PINN. Then, it provides the application of PINN in solving the look-ahead dispatch model for power systems.

A. PINN

The structure of the DNN applied in the present work follows that of the standard neural network shown in Fig. 1, which is a group of interconnected nodes connecting input and output layers via a total of K hidden layers, where the k^{th} hidden layer includes N_k neurons. Each neuron in the neural network is associated with a nonlinear activation function. In addition, each connection between neurons is associated with a weight w and a bias b, which are modified by the backpropagation algorithm during network training to minimize the mean square error (MSE) in the following loss function:

$$MSE = \frac{1}{M}\sum_{m=1}^{M}\left(y_m - \hat{y}_m\right)^2 \tag{56}$$

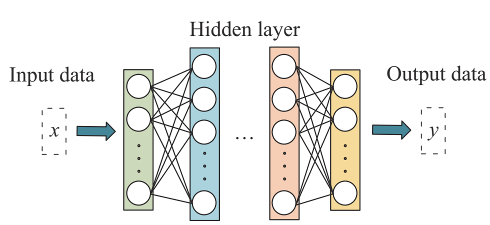

Fig. 1. Schematic architecture of a standard neural network.

The proposed PINN structure is illustrated in Fig. 2.

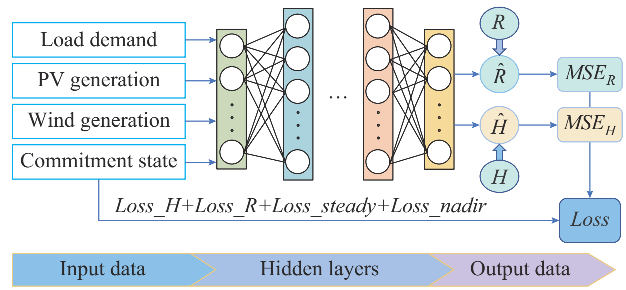

Fig. 2. Porposed PINN structure.

The process employed for training the PINN in this paper involves a modified loss function, which is based on the MSE obtained for the virtual inertia parameters H and droop control coefficients R of the RES and ESS units. Therefore, the loss function is rendered as:

$$MSE = MSE_H + MSE_R = \frac{1}{M}\left[\sum_{m=1}^{M}\left(\hat{R}_m - R_m\right)^2 + \sum_{m=1}^{M}\left(\hat{H}_m - H_m\right)^2\right] \tag{57}$$

In addition, we add the following penalties to the loss function to ensure that H and R meet the relevant constraints.

$$Loss\_H = \max\left(0, \hat{H} - H_{\max}\right) + \max\left(0, H_{\min} - \hat{H}\right) \tag{58}$$

$$Loss\_R = \max\left(0, \hat{R} - R_{\max}\right) + \max\left(0, R_{\min} - \hat{R}\right) \tag{59}$$

Finally, we add the following frequency-related constraints, including a steady-state frequency constraint and a nadir frequency constraint, to the loss function to ensure that the learned parameters are applicable to the original physical frequency dynamics model of the power system and meet the frequency constraints.

$$Loss\_steady = \max\left(0, \frac{\hat{R}\Delta P}{D\hat{R}+1} - \Delta f_{ss}\right) \tag{60}$$

$$Loss\_nadir = \max\left(0, \frac{\hat{R}\Delta P}{D\hat{R}+1}\left(1 + \hat{\alpha}e^{-\hat{\zeta}\hat{\omega}_n\hat{t}_{nadir}}\sqrt{1-\hat{\zeta}^2}\right) - \Delta f_{\max}\right) \tag{61}$$

This yields the following loss function for training the PINN.

$$\begin{aligned} Loss = MSE_R + MSE_H + \frac{1}{M}\big(&\alpha_1 Loss\_H + \alpha_2 Loss\_R + \\ &\alpha_3 Loss\_steady + \alpha_4 Loss\_nadir\big) \end{aligned} \tag{62}$$

The prediction performance of the PINN depends significantly on these weights. Therefore, these values must be selected appropriately to minimize the MSE effectively, as well as to reduce the chance of constraint violations.

B. Solution Process

Firstly, sample data pertaining to the H and R values of RES and ESS units, the active power demands, the reactive power demands, the RES outputs, and the commitment states of thermal generators for a representative power system are prepared for training and testing the PINN. Due to the challenge of obtaining a large volume of historical data, we utilize historical data from a specific region in Jiangsu

Province, China, in 2022 as a reference dataset. To ensure data diversity and universality, we use Python to generate 10950 load data points, where the loads stochastically fluctuate between 95% and 105% of their reference values. Additionally, we generate 10950 renewable energy data points, with RES outputs varying stochastically between 90% and 110% of their reference values. When applied to actual power systems, this approach anticipates that over time, training samples will accumulate a sufficient amount of historical data. The commitment states of thermal generators are generated based on solutions of the previously proposed frequency-constrained UC (FCUC) model [27]. Among these sample data, 80% are used for training, and the other 20% are used for testing. The appropriate parameters employed in the training process are listed, as shown in Table I, where training is conducted using Python 3.7 with Tensorflow.

TABLE I
NETWORK AND TRAINING PARAMETERS

Parameter	Numerical value	Parameter	Numerical value
Optimizer	Adam	Learning rate	1×10^{-3}
Training epoch	2000	Layer	5

The H and R values of each RES and ESS unit predicted by the PINN are then substituted into the proposed model, which makes the variable terms in (17)-(22) and constraints (24)-(31) constant. Thereby, the proposed model is transformed into a QCP form with quadratic terms only in the objective function and all other constraints being linear. The proposed model is then quickly and efficiently solved using the GUROBI solver in the general algebraic modeling system (GAMS).

IV. CASE STUDY

The effectiveness of the proposed model is evaluated based on numerical computations involving the test system, as shown in Fig. 3, which includes 54 conventional thermal generators, 5 PV stations at buses 19, 29, 39, 49, and 79, and 4 wind farms and 4 ESSs at buses 7, 11, 35, and 48. The relevant information of conventional units can be found in Supplementary Material B. The rated capacity of each RES unit is 500 MW. The detailed operation parameters of ESS units are listed in Table II. All case studies are performed on a laptop computer with an Intel Core i5-12500H CPU and 16 GB of RAM.

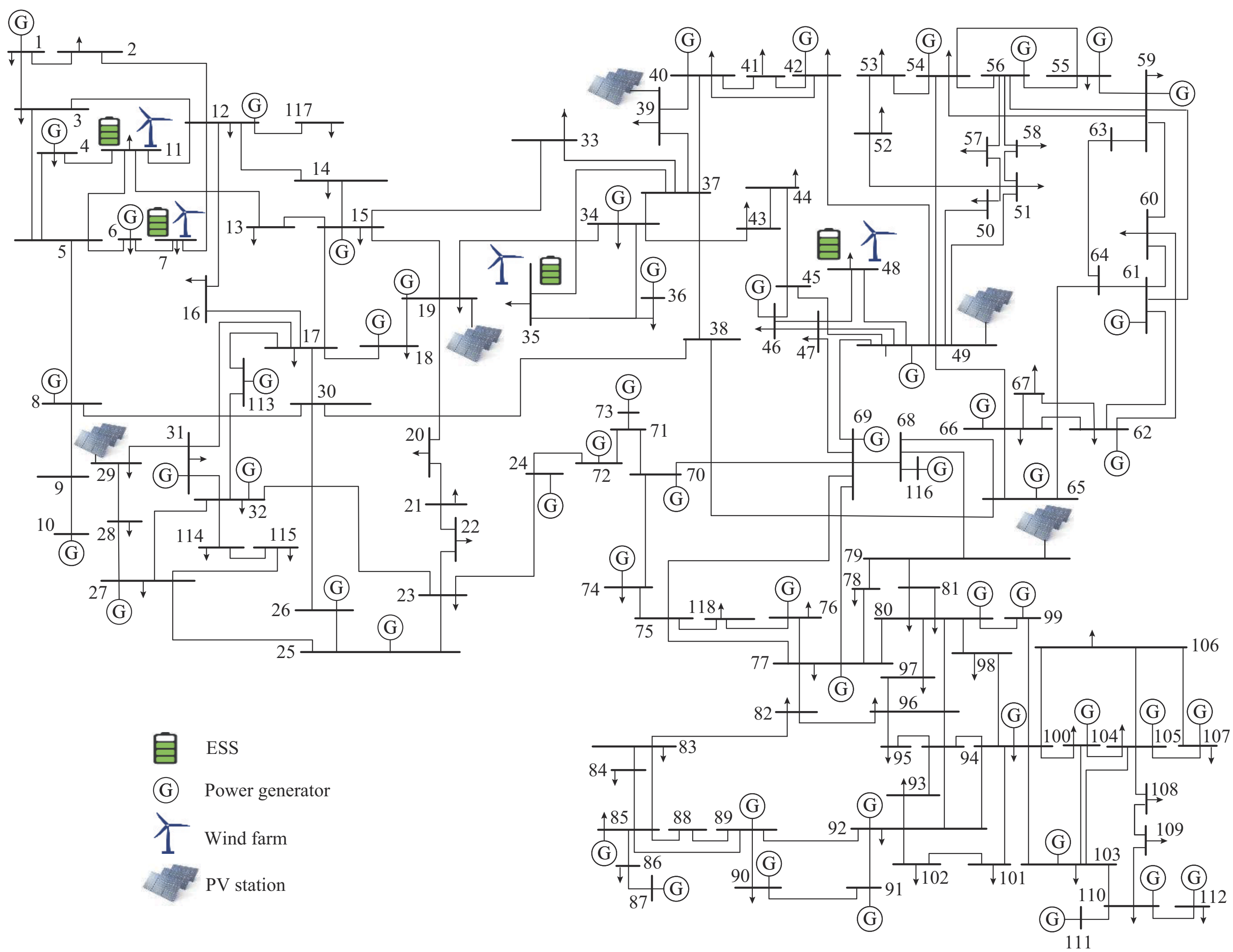

Fig. 3. Structure of test system.

The nominal system frequency f_0 is set to be 50 Hz, and the maximum allowable frequency deviation Δf_{max} and steady-state deviation Δf_{ss} are 0.5 Hz and 0.25 Hz, respectively. The parameters and range values of RES and ESS units are listed in Table III, where F represents fixed values applied in numerical calculations and V represents variable values. Unless otherwise specified, the power disturbance ΔP is set to be 0.10 of the current load demand.

TABLE II
OPERATION PARAMETERS OF ESS UNITS

Rated capacity (MWh)	The maximum charge/ discharge power (MW/h)	Initial state (MW)	Charge/ discharge efficiency (%)
240	100	200	96

TABLE III
PARAMETERS AND RANGE VALUES OF RES AND ESS UNITS

Type	Approach	H (s)	R
PV	F	2	0.067
	V	2-5	0.04-0.1
Wind farm	F	3	0.067
	V	2-5	0.04-0.1
ESS	F	4	0.067
	V	2-5	0.04-0.1

A. Impacts of Droop and Inertia Control on Frequency Response Curves

The effects of varying values of H and R on the frequency response of the test system are presented, as shown in Figs. 4 and 5, respectively, where the fixed value is applied for the non-variable term. As can be observed, H has a direct effect on the initial slope of the frequency response. The maximum deviation in the frequency of the test system from $f_0=50$ Hz decreases with increasing H, but the time t_{nadir} required for the test system to reach its frequency nadir f_{nadir} point gradually increases. Therefore, a larger value of H enhances the frequency stability of the test system. However, we note that H dose not affect the final steady-state frequency f_{ss}. Moreover, the frequency deviations observed under the varying values of H never exceed those established for f_{max} and f_{ss}, i.e., 49.5 Hz and 49.75 Hz, respectively, under the values of H considered. Meanwhile, the results in Fig. 5 indicate that the frequency stability of the test system improves with decreasing R, and the value of f_{ss} also increases. Moreover, the frequency deviations observed for R values of 0.08 and 0.09 exceed those established for f_{max} and f_{ss}. Therefore, a smaller value of R enhances the frequency stability of the test system.

B. Look-ahead Dispatch Results

The look-ahead dispatch results are evaluated for the test system under fixed values of H and R (scenario 1) and varying values of H and R (scenario 2) in conjunction with the net load demand and RES outputs presented in Fig. 6 over a 45 min time window during the day. Here, scenarios 1 and 2 effectively demonstrate the effects of including frequency constraints (24) and (25) in the proposed model.

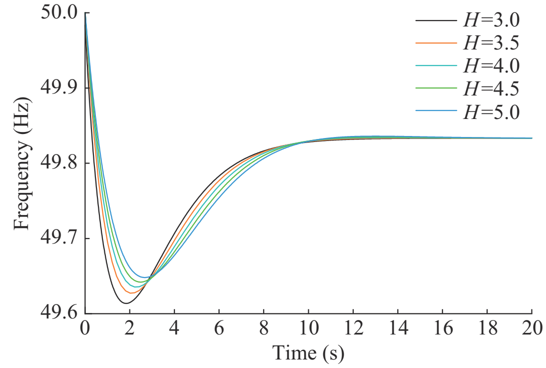

Fig. 4. Frequency response of test system for fixed R and varying values of H.

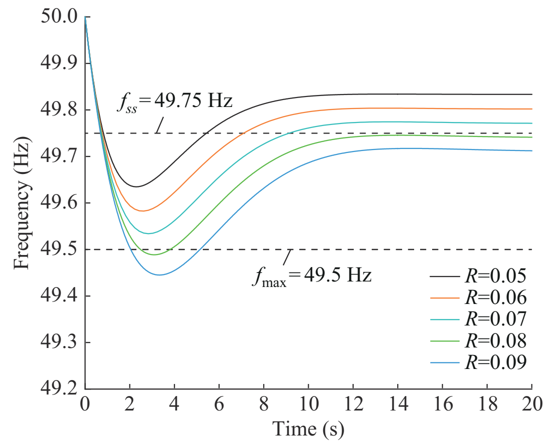

Fig. 5. Frequency response of test system for fixed H and varying values of R.

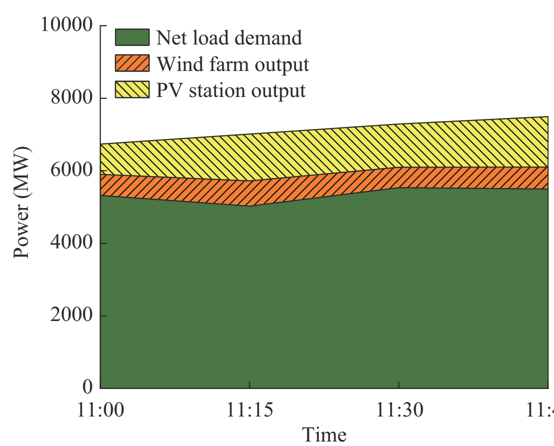

Fig. 6. Net load demand and RES output curves for test system.

The computation time required for solving the proposed model and the total operation cost obtained at $\Delta P=0.1$ for 45 min period in the two scenarios are listed, as shown in Table IV. The optimized H and R values obtained for wind farms, PV stations, and ESSs in scenario 2 are presented in the top and bottom rows of Fig. 7, respectively.

As can be observed from Table IV, the use of H and R values increases the computation time by almost an order of magnitude, and slightly increases the total operation cost of the test system by about 2%.

TABLE IV
COMPUTATION TIME REQUIRED FOR SOLVING PROPOSED MODEL AND TOTAL OPERATION COST WHEN $\Delta P=0.1$

Scenario	Computation time (s)	Total operation cost ($)
1	0.651	468623
2	6.471	478760

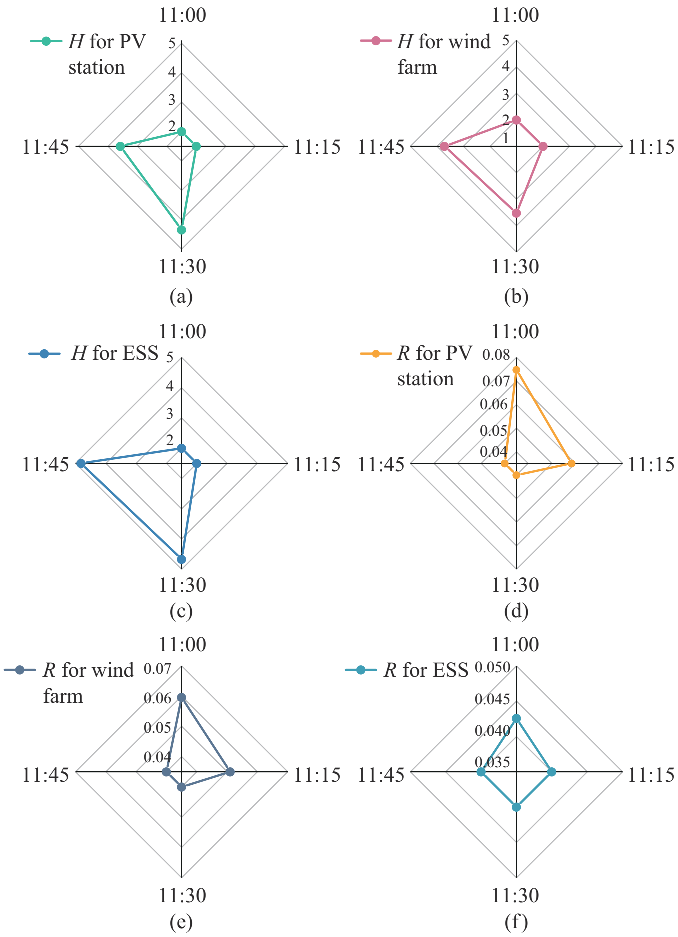

Fig. 7. H and R values in scenario 2 when $\Delta P=0.1$. (a) H for PV station. (b) H for wind farm. (c) H for ESS. (d) R for PV station. (e) R for wind farm. (f) R for ESS.

The increased computation time is an obvious effect of including constraints (24) and (25) in the proposed model. The slightly increased operation cost of the test system will be discussed later. In addition, the results in Fig. 7 clearly reflect the discussion in the preceding subsection of the effects of varying values of H and R on the frequency stability of the test system, where all values of H are high and all values of R are low during the period of relatively high load demand from 11:30 to 11:45.

The dynamic frequency response curves when $\Delta P=0.1$ are presented, as shown in Fig. 8. As can be observed, the use of fixed values of H and R in scenario 1 provides insufficient frequency support, while scenario 2 ensures that the test system consistently remains within a safe operation range. Of course, applying adjustable values of H and R in the dispatch process under this relatively high step disturbance inevitably increases the operation cost of the test system, as observed in Table IV, but the increase by 2% is not significant considering the benefit obtained.

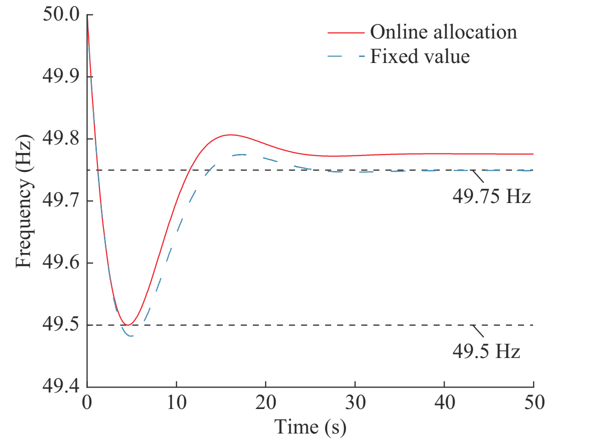

Fig. 8. Dynamic frequency response curves of test system when $\Delta P=0.1$ in scenarios 1 and 2 at 11:30.

The impact of the step disturbance on the results of the proposed model in scenarios 1 and 2 is evaluated further by applying a slightly smaller step disturbance when $\Delta P=0.09$ to the test system with the net load demand and RES outputs maintained at the levels presented in Fig. 6. The computation time required for solving the proposed model and total operation cost obtained for the 45-min period in the two scenarios are listed in Table V. The optimized values of H and R obtained for wind farms, PV stations, and ESSs in scenario 2 are presented in the top and bottom rows of Fig. 9, respectively, while the corresponding dynamic frequency response curves of the test system in the two scenarios are presented in Fig. 10.

TABLE V
COMPUTATION TIME REQUIRED FOR SOLVING PROPOSED MODEL AND TOTAL OPERATION COST WHEN $\Delta P=0.09$

Scenario	Computation time (s)	Total operation cost ($)
1	0.464	468623
2	6.043	461427

In contrast to what is observed in Table IV when $\Delta P=0.1$, the results in Table V indicate that the use of varying values of H and R slightly decreases the total operation cost of the test system by about 1.5% when ΔP is a slightly smaller value. Under this reduced disturbance condition, the conventional frequency support of thermal generators is sufficient to maintain a stable system frequency, as is illustrated in Fig. 9 by the uniformly small H value applied for all RES and ESS units over the entire 45-min period and the relatively large R value, which are still greater than the fixed value set in scenario 1 even at the high load level existing from 11:30 to 11:45. These settings avoid unnecessary RES curtailment required for regulating reserves, and can therefore reduce reserve costs and enhance the consumption of RES outputs. Additional reasons for the reduced operation cost of the test system under the proposed model are illustrated in Fig. 10.

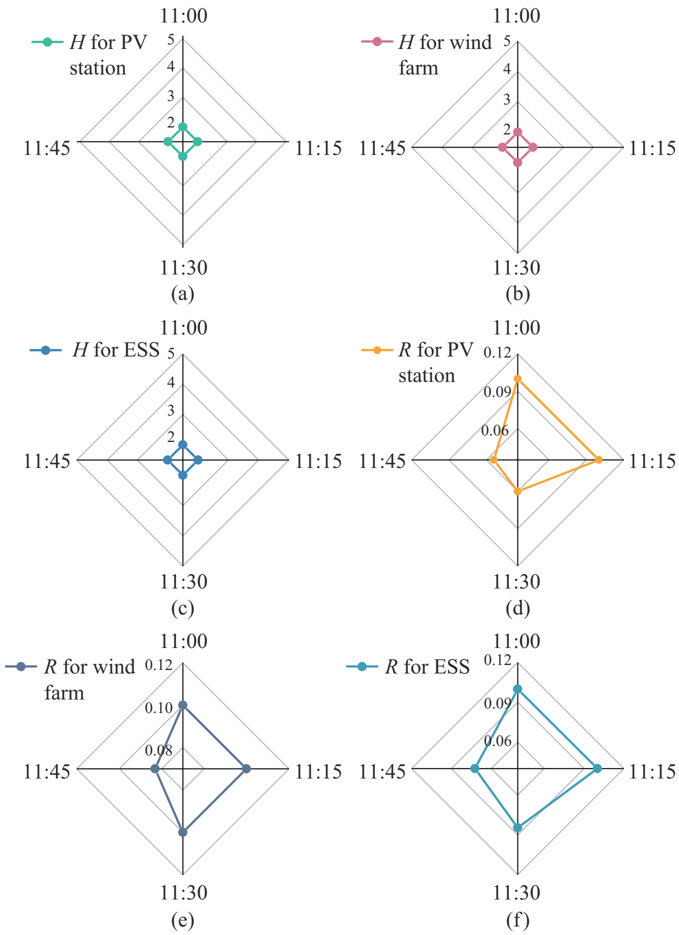

Fig. 9. Dispatch results of H and R in scenario 2 when $\Delta P=0.09$. (a) H for PV station. (b) H for wind farm. (c) H for ESS. (d) R for PV station. (e) R for wind farm. (f) R for ESS.

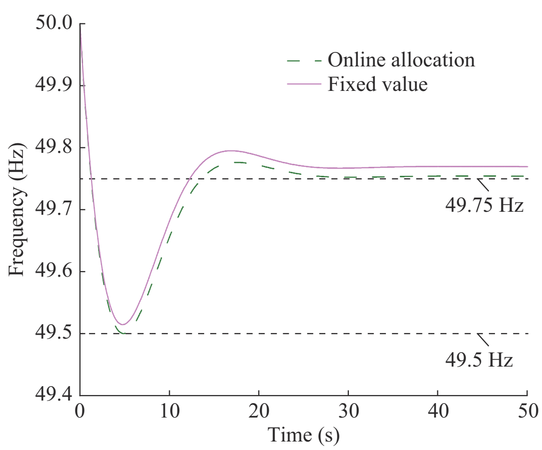

Fig. 10. Dynamic frequency response curves of test system when $\Delta P=0.09$ in scenarios 1 and 2 at 11:30.

The dispatch results meet the frequency requirements of the test system more precisely than the substantial margin for frequency regulation obtained in scenario 1, and therefore they reduce the operation cost of the test system.

The voltage amplitude at each bus of the test system in scenario 2 when $\Delta P=0.09$ over the period from 11:00 to 11:45 is presented in Fig. 11, along with the medium line and the mean voltage. It can be observed that the voltage amplitudes of each bus and time section lie within the specified allowable range ($0.94\leq\theta\leq 1.06$).

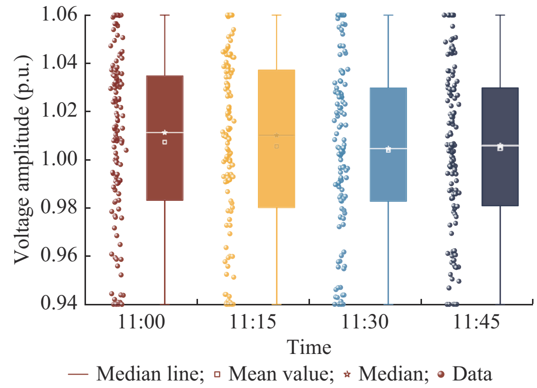

Fig. 11. Voltage amplitude at each bus in test system in scenario 2 when $\Delta P=0.09$.

C. Comparison of DL and PINNs

The same training dataset is applied for conducting three training sessions of the PINN and a DNN with an equivalent number of hidden layers, and the MSE and mean absolute percent error (MAPE) values obtained for H and R values predicted by the trained networks are compared for all three training sessions. In addition, the mean MSE (MMSE) and mean MAPE (MMAPE) values obtained over the three training sessions are also compared. The results are listed in Table VI. It can be observed that the MMSE of the PINN is 32% less than that obtained by the DNN, and the MMAPE is reduced by 25%.

TABLE VI
LEARNING PERFORMANCES OF DNN AND PINN ARCHITECTURES

Type	Number	MSE	MMSE	MAPE (%)	MMAPE (%)
	1	0.021		6.7	
DNN	2	0.020	0.0227	6.5	6.93
	3	0.027		7.6	
	1	0.015		5.0	
PINN	2	0.016	0.0153	5.3	5.20
	3	0.015		5.3	

The performance of the model and approach proposed in this paper is evaluated by solving the model with 5 randomly selected samples from the testing dataset, while employing the approach facilitated by predictions of H and R values obtained from the trained PINN and DNN, as well as a conventional physics-driven (PD) approach [14]. The total operation costs and computation time of the approaches are listed in Tables VII and VIII, respectively. In Table VII, the data within the brackets indicate the percentage by which the total cost of the neural network-assisted approach exceeds that of the physically-driven approach. The data within the brackets in Table VIII indicate the increase in the solution speed achieved by the neural network-assisted approach relative to the physically-driven approach. As can be observed, the operation cost obtained using either the PINN or DNN in the solution process is greater than that obtained using the PD approach. However, the additional operation cost does not exceed 1%. Moreover, the use of machine learning dramatically decreases the computation time from seconds or even minutes to tenths of a second. In fact, the solution speed of case 1 has increased by more than 300 times.

TABLE VII
COMPARISON OF TOTAL OPERATION COST OBTAINED FOR TEST SYSTEM FROM SOLUTION PROCESS USING VALUES PREDICTED BY VARIOUS NEURAL NETWORKS

Case	Cost ($)		
	DNN	PINN	PD
1	444022 (↑ 0.33%)	444913 (↑ 0.53%)	442580
2	414599 (↑ 0.56%)	414684 (↑ 0.58%)	412298
3	325297 (↑ 0.86%)	322588 (↑ 0.02%)	322522
4	337756 (↑ 0.03%)	337940 (↑ 0.08%)	337670
5	453735 (↑ 0.21%)	455771 (↑ 0.66%)	452781

TABLE VIII
COMPARISON OF COMPUTATION TIME

Case	Time (s)		
	DNN	PINN	PD
1	0.400 (↓ 343.8×)	0.423 (↓ 325.1×)	137.537
2	0.877 (↓ 5.6×)	0.729 (↓ 6.7×)	4.909
3	0.759 (↓ 7.4×)	0.785 (↓ 7.2×)	5.628
4	0.423 (↓ 24.2×)	0.466 (↓ 21.9×)	10.222
5	0.444 (↓ 21.9×)	0.432 (↓ 22.5×)	9.741

However, the results observed for the machine learning approaches in Tables VII and VIII present no clearly discernible trends regarding the impact of the selected network on the operation costs or computation time. Therefore, the advantages and disadvantages of using different neural networks are further compared by analyzing the frequency control performance obtained by the proposed model when solved for the test system over the period from 11:00 to 11:45 when $\Delta P = 0.09$ using the DNN- and PINN-assisted approaches, as shown in Figs. 12 and 13, respectively. In addition, the proposed model is solved over five independent trials, and the frequency nadir deviation and steady-state frequency deviation values obtained for each trial over each 15-min period are evaluated in Figs. 12(a), 12(b), 13(a), and 13(b), respectively. The circled boxes in Fig. 12 represent breaches in the frequency constraint. Accordingly, the model solved using the DNN-assisted approach violates the f_{nadir} constraint in cases 1, 2, and 5, while the f_{ss} constraint is violated in case 4. It must be noted that such deviations cannot be tolerated in actual power system operation because this may lead to unstable system operation and even system collapse. In contrast, applying the PINN-assisted approach ensures that the power system remains consistent in a safe operation state. The frequency control performances obtained by the proposed model when solved with parameter values predicted by the different networks can be attributed to the greater prediction performance of the PINN observed in Section IV-C relative to that of the DNN, as shown in Table VI.

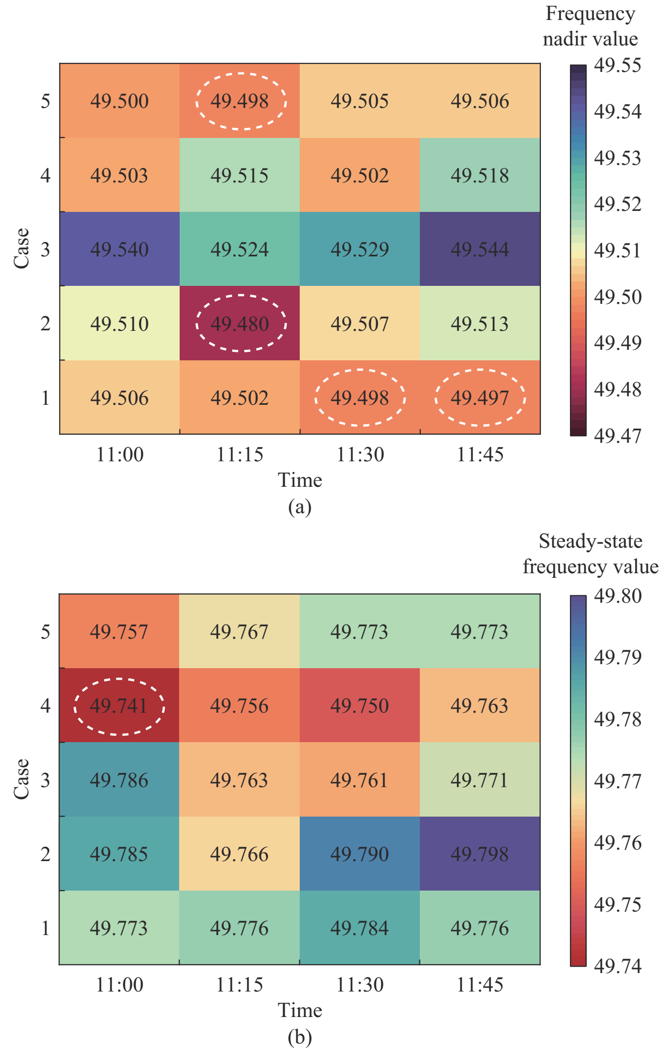

Fig. 12. Frequency control performance of proposed model applied to test system over five different trials when being solved using DNN-assisted approach. (a) Frequency nadir value. (b) Steady-state frequency value.

V. CONCLUSION

This paper proposes a look-ahead dispatch model of power systems based on linear AC-OPF framework with nonlinear frequency constraints using PINNs. The PINN-assisted approach provides an accurate estimation of H and R, thus greatly reducing the computation burden of the traditional model-based look-ahead scheduling model. The main contributions are summarized as follows.

1) The results of numerical computations for the test system demonstrate that the proposed model can reduce operation costs while ensuring frequency safety under a small power disturbance when $\Delta P = 0.09$.

2) The frequency safety can be ensured under a larger power disturbance when $\Delta P = 0.1$ with very modest cost increase by adjusting the H and R values of RES and ESS units.

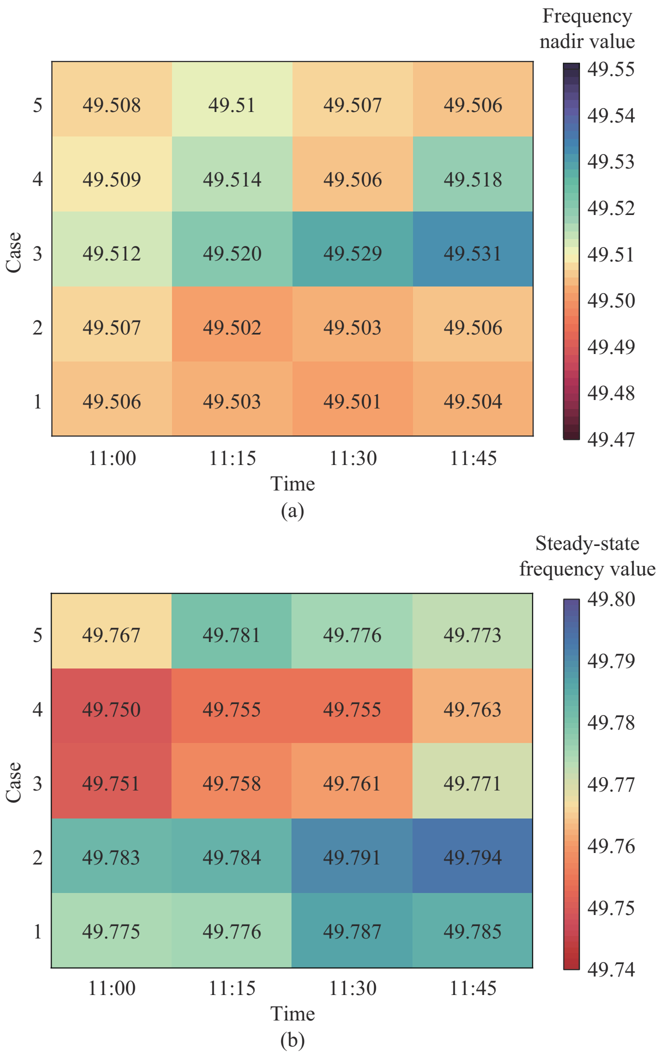

Fig. 13. Frequency control performance of proposed model applied to test system over five different trials when being solved using PINN-assisted approach. (a) Frequency nadir value. (b) Steady-state frequency value.

3) The use of machine learning is demonstrated to decrease the computation time required for solving the proposed model dramatically from seconds or even minutes to tenths of a second.

4) The trained PINN is demonstrated to provide greater prediction performance for H and R values than an equivalently trained DNN with a similar architecture. This prediction performance is found to eliminate violations in the frequency constraints, where the use of the DNN produces numerous violations that cannot be tolerated in actual power system operation.

A frequency- or inertia-based ancillary service market can be established to incentivize generator/energy storage/RES to provide inertia support, which will be part of our future work.

References

[1] H. Xu, B. Feng, C. Wang *et al.*, "Exact box-constrained economic operating region for power grids considering renewable energy sources," *Journal of Modern Power Systems and Clean Energy*, vol. 12, no. 2, pp. 514-523, Mar. 2024.

[2] K. Das, F. Guo, E. Nuño *et al.*, "Frequency stability of power system with large share of wind power under storm conditions," *Journal of Modern Power Systems and Clean Energy*, vol. 8, no. 2, pp. 219-228, Mar. 2020.

[3] L. Xie, P. M. S. Carvalho, L. A. F. M. Ferreira *et al.*, "Wind integration in power systems: operational challenges and possible solutions," *Proceedings of the IEEE*, vol. 99, no. 1, pp. 214-232, Jan. 2011.

[4] C. Zhang, L. Liu, H. Cheng *et al.*, "Frequency-constrained co-planning of generation and energy storage with high-penetration renewable energy," *Journal of Modern Power Systems and Clean Energy*, vol. 9, no. 4, pp. 760-775, Jul. 2021.

[5] J. Zhang, Z. Chen, N. Zhang *et al.*, "Frequency-constrained unit commitments with linear rules extracted from simulation results considering regulations from battery storage," *Journal of Modern Power Systems and Clean Energy*, vol. 11, no. 4, pp. 1041-1052, Jul. 2023.

[6] L. Wang, H. Fan, J. Liang *et al.*, "Multi-area frequency-constrained unit commitment for power systems with high penetration of renewable energy sources and induction machine load," *Journal of Modern Power Systems and Clean Energy*, vol. 12, no. 3, pp. 754-766, May 2024.

[7] Y.-K. Wu, S.-M. Chang, and P. Mandal, "Grid-connected wind power plants: a survey on the integration requirements in modern grid codes," *IEEE Transactions on Industry Applications*, vol. 55, no. 6, pp. 5584-5593, Nov. 2019.

[8] A. H. A. El-Kareem, M. A. Elhameed, and M. M. Elkholy, "Effective damping of local low frequency oscillations in power systems integrated with bulk PV generation," *Protection and Control Modern Power Systems*, vol. 6, no. 4, pp. 512-524, Dec. 2021.

[9] Z. Li, W. Wu, B. Zhang *et al.*, "Efficient location of unsatisfiable transmission constraints in look-ahead dispatch via an enhanced lagrangian relaxation framework," *IEEE Transactions on Power Systems*, vol. 30, no. 3, pp. 1233-1242, May 2015.

[10] J. Liu, C. Wang, J. Zhao *et al.*, "RoCoF constrained unit commitment considering spatial difference in frequency dynamics," *IEEE Transactions on Power Systems*, vol. 39, no. 1, pp. 1111-1125, Jan. 2024.

[11] S. Chen, A. J. Conejo, R. Sioshansi *et al.*, "Unit commitment with an enhanced natural gas-flow model," *IEEE Transactions on Power Systems*, vol. 34, no. 5, pp. 3729-3738, Sept. 2019.

[12] W. Zheng, Z. Li, and H. Zhou, "Efficient robust look-ahead dispatch incorporating critical region preparation in gap time," *IEEE Transactions on Power Systems*, vol. 36, no. 5, pp. 4840-4843, Sept. 2021.

[13] B. K. Poolla, A. R. Hota, S. Bolognani *et al.*, "Wasserstein distributionally robust look-ahead economic dispatch," *IEEE Transactions on Power Systems*, vol. 36, no. 3, pp. 2010-2022, May 2021.

[14] Y. Shen, W. Wu, B. Wang *et al.*, "Optimal allocation of virtual inertia and droop control for renewable energy in stochastic look-ahead power dispatch," *IEEE Transactions on Sustainable Energy*, vol. 14, no. 3, pp. 1881-1894, Jul. 2023.

[15] C. Liu, H. Zhang, M. Shahidehpour *et al.*, "A two-layer model for microgrid real-time scheduling using approximate future cost function," *IEEE Transactions on Power Systems*, vol. 37, no. 2, pp. 1264-1273, Mar. 2022.

[16] M. Maluenda, S. Córdova, A. Lorca *et al.*, "Optimal operation scheduling of a PV-BESS-electrolyzer system for hydrogen production and frequency regulation," *Applied Energy*, vol. 344, Aug. 2023.

[17] A. J. Wood, B. F. Wollenberg, and G. B. Sheblé, *Power Generation, Operation and Control*. New York: Wiley, 1996.

[18] Z. Yang, H. Zhong, A. Bose *et al.*, "A linearized OPF model with reactive power and voltage magnitude: a pathway to improve the MW-only DC OPF," *IEEE Transactions on Power Systems*, vol. 33, no. 2, pp. 1734-1745, Mar. 2018.

[19] M. I. A. Shekeew and B. Venkatesh, "Learning-assisted variables reduction method for large-scale MILP unit commitment," *IEEE Open Access Journal of Power and Energy*, vol. 10, pp. 245-258, Oct. 2023.

[20] W. Huang, X. Pan, M. Chen *et al.*, "DeepOPF-V: solving AC-OPF problems efficiently," *IEEE Transactions on Power Systems*, vol. 37, no. 1, pp. 800-803, Jan. 2022.

[21] J. Liu, H. Zang, L. Cheng *et al.*, "A transformer-based multimodal-learning framework using sky images for ultra-short-term solar irradiance forecasting," *Applied Energy*, vol. 342, p. 121160, Jul. 2023.

[22] Y. Zhang, Z. Pan, H. Wang *et al.*, "Achieving wind power and photovoltaic power prediction: an intelligent prediction system based on a deep learning approach," *Energy*, vol. 283, p. 129005, Nov. 2023.

[23] M. Zhou, M. Chen, and S. H. Low, "DeepOPF-FT: one deep neural network for multiple AC-OPF problems with flexible topology," *IEEE Transactions on Power Systems*, vol. 38, no. 1, pp. 964-967, Jan. 2023.

[24] P. M. Anderson and M. Mirheydar, "A low-order system frequency re-

sponse model," *IEEE Transactions on Power Systems*, vol. 5, no. 3, pp. 720-729, Aug. 1990.

[25] Q. Shi, F. Li, and H. Cui, "Analytical method to aggregate multi-machine SFR model with applications in power system dynamic studies," *IEEE Transactions on Power Systems*, vol. 33, no. 6, pp. 6355-6367, Nov. 2018.

[26] J. F. Restrepo and F. D. Galiana, "Unit commitment with primary frequency regulation constraints," *IEEE Transactions on Power Systems*, vol. 20, no. 4, pp. 1836-1842, Nov. 2005.

[27] Z. Zhang, E. Du, F. Teng *et al*., "Modeling frequency dynamics in unit commitment with a high share of renewable energy," *IEEE Transactions on Power Systems*, vol. 35, no. 6, pp. 4383-4395, Nov. 2020.

[28] Y. Yuan, Y. Zhang, J. Wang *et al*., "Enhanced frequency-constrained unit commitment considering variable-droop frequency control from converter-based generator," *IEEE Transactions on Power Systems*, vol. 38, no. 2, pp. 1094-1110, Mar. 2023.

[29] H. Li, Y. Qiao, Z. Lu *et al*., "Frequency-constrained stochastic planning towards a high renewable target considering frequency response support from wind power," *IEEE Transactions on Power Systems*, vol. 36, no. 5, pp. 4632-4644, Sept. 2021.

[30] X. Zhao, H. Wei, J. Qi *et al*., "Frequency stability constrained optimal power flow incorporating differential algebraic equations of governor dynamics," *IEEE Transactions on Power Systems*, vol. 36, no. 3, pp. 1666-1676, May 2021.

[31] N. Yang, C. Yang, C. Xing *et al.*, "Deep learning-based SCUC decision-making: an intelligent data-driven approach with self-learning capabilities," *IET Generation, Transmission and Distribution*, vol. 16, no. 4, pp. 629-640, Apr. 2022.

[32] B. Huang and J. Wang, "Applications of physics-informed neural networks in power systems – a review," *IEEE Transactions on Power Systems*, vol. 38, no. 1, pp. 572-588, Jan. 2023.

[33] R. Nellikkath and S. Chatzivasileiadis, "Physics-informed neural networks for AC optimal power flow," *Electric Power Systems Research*, vol. 212, p. 108412, Nov. 2022.

[34] X. Hu, H. Hu, S. Verma *et al*., "Physics-guided deep neural networks for power flow analysis," *IEEE Transactions on Power Systems*, vol. 36, no. 3, pp. 2082-2092, May 2021.

[35] M. E. C. Bento, "Physics-guided neural network for load margin assessment of power systems," *IEEE Transactions on Power Systems*, vol. 39, no. 1, pp. 564-575, Jan. 2024.

[36] S. Zhang, W. Gu, X. Zhang *et al.*, "Steady-state security region of integrated energy system considering thermal dynamics," *IEEE Transactions on Power Systems*, vol. 39, no. 2, pp. 4138-4153, Mar. 2024.

[37] Z. Yang, H. Zhong, Q. Xia *et al.*, "Optimal power flow based on successive linear approximation of power flow equations," *IET Generation, Transmission and Distribution*, vol. 10, no. 14, pp. 3654-3662, Nov. 2016.

[38] Z. Yang, A. Bose, H. Zhong *et al.*, "Optimal reactive power dispatch with accurately modeled discrete control devices: a successive linear approximation approach," *IEEE Transactions on Power Systems*, vol. 32, no. 3, pp. 2435-2444, May 2017.

Guoqiang Sun received the B.S., M.S., and Ph.D. degrees in electrical engineering from Hohai University, Nanjing, China, in 2001, 2005, and 2010, respectively. He was a Visiting Scholar with North Carolina State University, Raleigh, USA, from 2015 to 2016. He is currently a Professor with the College of Energy and Electrical Engineering, Hohai University. His research interests include power system analysis and economic dispatch and optimal control of integrated energy systems.

Qihui Wang received the B.S. degree from the College of Energy and Electrical Engineering, Hohai University, Nanjing, China, in 2022. Hi is currently pursuing the M.S. degree from the College of Energy and Electrical Engineering, Hohai University, Nanjing, China. Her research interests include unit commitment, machine learning, and optimal operation of power system.

Sheng Chen received the B.S. and Ph.D. degrees from the College of Energy and Electrical Engineering, Hohai University, Nanjing, China, in 2014 and 2019, respectively. From January 2018 to January 2019, he was a Visiting Scholar at The Ohio State University, Columbus, USA. He is currently a Professor in the College of Energy and Electrical Engineering, Hohai University. He serves as an Associate Editor of the Journal of Modern Power Systems and Clean Energy. His research interests include integrated energy system, operation research, and electricity market.

Zhinong Wei received the B.S. degree from Hefei University of Technology, Hefei, China, in 1984, the M.S. degree from Southeast University, Nanjing, China, in 1987, and the Ph.D. degree from Hohai University, Nanjing, China, in 2004. He is currently a Professor of electrical engineering with the College of Energy and Electrical Engineering, Hohai University. His research interests include integrated energy system, power system state estimation, smart distribution system, and integration of distributed generation into electric power systems.

Haixiang Zang received the B.S. degree in electrical engineering from Nanjing Normal University, Nanjing, China, in 2009, and the Ph.D. degree in electrical engineering from Southeast University, Nanjing, China, in 2014. He is currently an Associate Professor with the College of Energy and Electrical Engineering, Hohai University, Nanjing, China. His research interests include generation of renewable energy, and operation and control of power system.